Journal of Luminescence 128 (2008) 2013–2018

Contents lists available at ScienceDirect

Journal of Luminescence

journal homepage: www.elsevier.com/locate/jlumin

Luminescence properties of $Ce^{3+}$and Tb^{3+} ions codoped strontium borate phosphate phosphors

Fang Wang [a,b], Hongwei Song [c,*], Guohui Pan [a,b], Libo Fan [a,b], Biao Dong [a,b], Lina Liu [a,b], Xue Bai [a,b], Ruifei Qin [a,b], Xinguang Ren [a,b], Zhuhong Zheng [a,b], Shaozhe Lu [a,b]

[a] Key Laboratory of Excited State Physics, Changchun Institute of Optics, Fine Mechanics and Physics, Chinese Academy of Sciences, 16 Eastern South-Lake Road, Changchun 130033, People's Republic of China

[b] Graduate School of Chinese Academy of Sciences, Beijing 100039, People's Republic of China

[c] State Key Laboratory of Integral Optoelectronics, College of Electronic Science and Engineering, JiLin University, Changchun 130012, People's Republic of China

ARTICLE INFO

Article history:
Received 27 June 2007
Received in revised form
25 January 2008
Accepted 24 June 2008
Available online 1 July 2008

Keywords:
$2SrO–nB_2O_3–(1-n)P_2O_5:Ce^{3+}$, Tb^{3+}
Photoluminescence
Energy transfer

ABSTRACT

The Ce^{3+}-activated, Tb^{3+}-activated, and Ce^{3+} and Tb^{3+} co-activated phosphors $2SrO–nB_2O_3–(1-n)P_2O_5$ were synthesized by the solid-state reaction. The structures, photoluminescent spectra and dynamics of them were systemically studied. The results demonstrate that the structure of the samples with $n = 0.10–0.50$ belongs to the hexagonal phase. When n is beyond this range, the structures are the mixed phases of α-$Sr_2P_2O_7$ and $Sr_2B_2O_5$. The optimum composition is determined to be $n = 0.25$ for the $2SrO–nB_2O_3–(1-n)P_2O_5$ phosphors. As n varies from 0.01 to 0.50, the lifetime of Ce^{3+} ion increases gradually, while the lifetime of Tb^{3+} ion decreases, indicating that the energy transfer efficiency decreases with the increase of n. The ET efficiency between Ce^{3+} and Tb^{3+} in the optimum composition reaches to 70%. The present results demonstrate that the Ce^{3+} and Tb^{3+} co-activated hexagonal $2SrO–0.25B_2O_3–0.75P_2O_5$ powders can possibly be applied as the newly developed green efficient phosphors in the field of lighting and display.

1. Introduction

The rare earth ions activated materials are widely used as lamp phosphors, cathode ray tube phosphors and scintillator phosphors, because of their unique spectroscopic properties [1,2]. New hosts doped with rare earth ions are getting much attention owing to their potential applications. Recently, the considerable variety in crystal structure of the borophosphate compounds provides a great deal of objects for the study aiming at exploring new functional materials. As far as luminescence is concerned, attention has been brought to alkaline earth borophosphate lattices doped with rare earth ions, because it has high luminescence, moderately synthetical temperature, great X color coordinate and low thermal degradation. Generally, the alkaline earth borophosphates are reported to be isostructural with mineral stillwellite, which are built up with BO_4 and PO_4 tetrahedra. The ions are coordinated with nine oxygen ions with C_2 symmetry [3,4]. The basic anionic constituents of these compounds are recommended to be interpreted in terms of BPO_4 groups, i.e. PO_4^+–BO_4^-, where B and P are four-coordinated [5,6]. The alkaline earth borophosphates are built up with BO_4 and PO_4 tetrahedra, which formed three-dimensional net-like structures. The structures of these borophosphates can keep rare earth ions from oxidation because of their stable structures. Blasse first reported the UV-excited blue emission of Eu^{2+} in $MBPO_5:Eu^{2+}$ (M = Ca, Sr, Ba) [7]. Verwey et al. studied the luminescence properties of divalent europium in crystalline and glass modification of calcium borophosphate [8]. Karthikeyani and Jagannathan prepared the X-ray storage phosphor $SrBPO_5:Eu^{2+}$ [4]. Previously, the studies on luminescence properties of rare earth ions in the $MBPO_5$ host were mainly focused on divalent Eu^{2+} and Sm^{2+} [4,9–11], which mainly based on the 4f–5d transitions of the rare earths.

Ce^{3+} and Tb^{3+} ions are important trivalent RE ions, which have been applied in blue and green phosphors. Cerium and terbium ions doped materials are of great importance because of their practical application in lighting and display. The energy transfer (ET) processes between Ce^{3+} and Tb^{3+} in different hosts, such as lanthanum oxybromide [12], aluminate [13], alkaline earth sulfate [14] and so on, are intensively investigated. However, the studies on luminescence dynamics, ET processes between Ce^{3+} and Tb^{3+}in these alkaline earth borophosphate systems have not been investigated. In this paper, we systemically synthesize the green-emitting phosphors $2SrO–nB_2O_3–(1-n)P_2O_5:Ce^{3+},Tb^{3+}$ by the solid-state reaction and systemically study on their photoluminescence properties.

* Corresponding author. Fax: +86 431 86176320.
E-mail address: hwsong2005@yahoo.com.cn (H. Song).

0022-2313/$ - see front matter © 2008 Elsevier B.V. All rights reserved.
doi:10.1016/j.jlumin.2008.06.012

2. Experimental

2.1. Sample preparation

$2SrO–nB_2O_3–(1-n)P_2O_5$:1%Ce^{3+},2.5%Tb^{3+} phosphors were prepared by the solid-state reaction at high temperature. The starting materials were analytical grade $Sr(NO_3)_2$, $Tb(NO_3)_3 \cdot 5H_2O$ (purity 99.99%), $Ce(NO_3)_3 \cdot 5H_2O$ (purity 99.99%), H_3BO_3 (excess 3 mol% to compensate the evaporation) and $(NH_4)_2HPO_4$ with different proportion between $(NH_4)_2HPO_4$ and H_3BO_3. Two annealing steps were necessary for synthesizing the samples. First, stoichiometeric amount of the starting materials were thoroughly mixed and annealed at 400 °C for 4 h, and subsequently annealed in air at 1000 °C for another 4 h in a covered aluminum oxide crucible. After these steps, the temperature was slowly reduced to room temperature. Finally, the white powders of $2SrO–nB_2O_3–(1-n)P_2O_5$:1%Ce^{3+},2.5%Tb^{3+} were obtained.

To obtain the optimum composition, which was doped with different (Ce^{3+}or Tb^{3+}) concentration and study the dependence of ET processes between Ce^{3+} and Tb^{3+} on concentration, the amount of $Ce(NO_3)_3 \cdot 5H_2O$ or $Tb(NO_3)_3 \cdot 5H_2O$ was adjusted in the preparation.

2.2. Measurements

The crystal structures were obtained by X-ray diffraction (XRD) using a Cu target radiation resource ($\lambda = 1.54078$ Å). The excitation and emission spectra at room temperature were measured with a Hitachi F-4500 fluorescence spectrometer. In the measurements of fluorescence dynamics of Tb^{3+}, a 355 nm light generated from the Fourth-Harmonic-Generator pumped by the pulsed Nd:YAG laser was used as excitation source. It is with a line width of 1.0 cm^{-1}, pulse duration of 10 ns and repetition frequency of 10 Hz. The spectra were recorded by a Spex-1403 spectrometer, a photomultiplier and a boxcar integrator and processed by a computer. The fluorescence dynamics of Ce^{3+} were measured with a FL920 single-photon spectrometer using a nanosecond flash-lamp as the excitation source, which is with a pulse width of 1 ns and a repetition rate of 40 kHz.

3. Results and discussion

3.1. Structure of the $2SrO–nB_2O_3–(1-n)P_2O_5$ powders

Fig. 1 shows the X-ray diffraction patterns (XRD) of different $2SrO–nB_2O_3–(1-n)P_2O_5$:1%Ce^{3+},2.5%Tb^{3+} samples in contrast to the standard card of orthorhombic α-$Sr_2P_2O_7$ (JCPDS no. 24-1011), monoclinic $Sr_2B_2O_5$ (JCPDS no. 73-1930) and strontium borate phosphate (JCPDS no. 18-1270). For the α-$Sr_2P_2O_7$ sample ($n = 0$), all the XRD lines match the lines given in no. 24-1011 of JCPDS data files. It can be found that the structure of the powder is in pure orthorhombic phase (α-$Sr_2P_2O_7$). The unit cell parameters obtained are $a = 8.917$ Å, $b = 13.16$ Å, $c = 5.400$ Å, respectively. The structure of $Sr_2B_2O_5$ ($n = 1$) is in pure monoclinic phase, which is similar to that reported for the compound strontium borate (JCPDS no. 73-1930). As for the $n = 0.01$ and 0.90 samples, the results indicate that there exist the mixed phases of the α-$Sr_2P_2O_7$ and $Sr_2B_2O_5$ in both the two samples, as shown in Fig. 1. As n varies from 0.10 to 0.50, the XRD patterns are similar to that reported for the compound strontium borate phosphate (JCPDS no. 18-1270). As the value of n varies from 0.10 to 0.50, the crystal structure of the samples can be indexed to the hexagonal space groups. In contrast to the standard cards, the XRD patterns in the present samples become broader to different degree. It may be attributed to the different structure between BO_4^- and PO_4^-, which leads to the inhomogeneous structure distribution. Therefore, there is considerable line broadening, indicating lattice strain, in the diffraction patterns of the mixed borate and phosphate compounds [15].

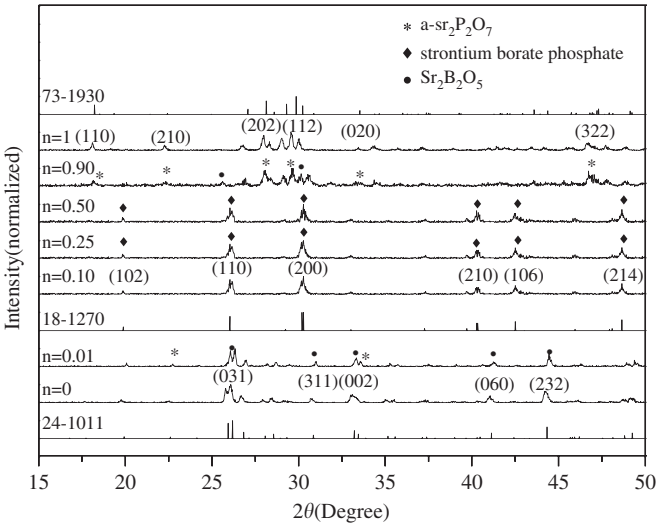

Fig. 1. The X-ray diffraction patterns (XRD) in different $2SrO–nB_2O_3–(1-n)P_2O_5$: 1%Ce^{3+},2.5%Tb^{3+} samples and the JCPDS card 24-1011 for α-$Sr_2P_2O_7$, the JCPDS card 18-1270 for compound strontium borate phosphate and the JCPDS card 73-1930 for $Sr_2B_2O_5$.

3.2. The luminescence properties of $2SrO–nB_2O_3–(1-n)P_2O_5$:1%Ce^{3+},2.5%Tb^{3}

Fig. 2(a) gives the excitation (left) and emission spectra (right) of Ce^{3+}-activated $2SrO–0.25B_2O_3–0.75P_2O_5$ powders. It can be seen that the excitation spectrum consists of three components, having peaks at 258, 266 and 286 nm (the strongest), respectively, which corresponds to the transitions from the ground-state $^2F_{5/2}$ of Ce^{3+} to different crystal-field components of the excited Ce^{3+}5d states. The emission band of Ce^{3+} consists of a broadband with a maximum at 326 nm and a shoulder at 340 nm, which are the characteristic splitting of the emission bands of Ce^{3+}due to the spin–orbit split of the ground state. These bands should correspond to the 5d–^2F_J ($J = 7/2$, 5/2) transitions of Ce^{3+}. The energy difference between the two peaks is ~1263 cm^{-1}, which is basically in accordance with the ground state splitting of Ce^{3+} (2000 cm^{-1}, i.e., energy difference between $^2F_{5/2}$ and $^2F_{7/2}$ doublets in the $4f^1$ configuration of the Ce^{3+} ion) [16].

The rare earth ions were reported to occupy the crystal lattice sites with C_2 symmetry in iso-structural host $MBPO_5$ (M = Ca, Sr) [10,17,18]. Berezovskaya et al. reported the UV excitation spectrum of Ce^{3+} in the $SrBPO_5$ host recently. They observed that the 5d orbits split into sublevels in the range of 230–290 nm and the crystal-field components of the excited 5d configuration located at 241, 258 and 277 nm, respectively [19]. Compared with their result, the excitation spectrum of Ce^{3+} in the present sample shifts to red, which points to a stronger relaxation in the 5d excited state of Ce^{3+} in the $2SrO–0.25B_2O_3–0.75P_2O_5$ host.

Fig. 2(b) exhibits the excitation (left) and emission spectra (right) in Tb^{3+}-activated $2SrO–0.25B_2O_3–0.75P_2O_5$ powders. A number of excitation lines of Tb^{3+} ions exist in UV range, which is associated with $^7F_6–^5D_3$, $^7F_6–^5G_J$ and $^7F_6–^5L_6$ transitions of Tb^{3+}. The emission lines from 480 to 650 nm are associated with the $^5D_4–^7F_J$ ($J = 3–6$) transitions. Among them, the green $^5D_4–^7F_5$ emission at 541 nm is the strongest.

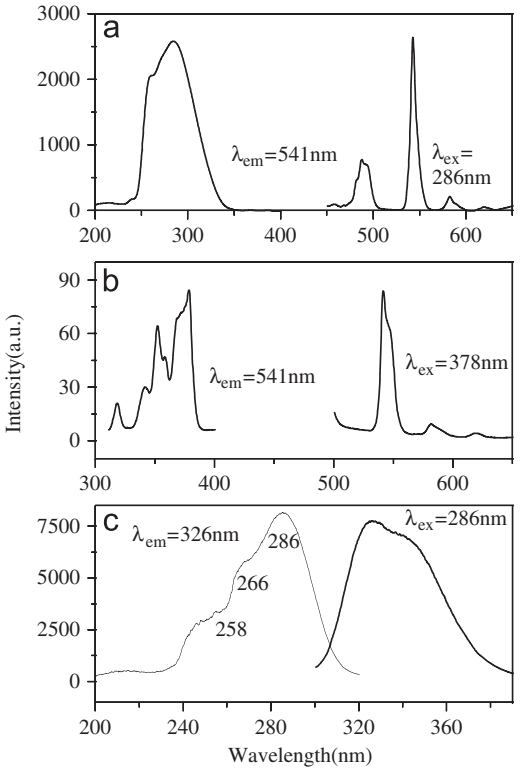

Fig. 2. (a) The excitation (left) and emission spectra (right) for Ce^{3+}-activated $2SrO–0.25B_2O_3–0.75P_2O_5$ powders. (b) The excitation (left) and emission spectra (right) in Tb^{3+}-activated $2SrO–0.25B_2O_3–0.75P_2O_5$ powders. (c) The excitation (left) and emission spectra (right) in Ce^{3+}/Tb^{3+}-coactivated $2SrO–0.25B_2O_3–0.75P_2O_5$ powders.

Fig. 2(c) shows the excitation (left) and emission spectra (right) in Ce^{3+}/Tb^{3+}-coactivated $2SrO–0.25B_2O_3–0.75P_2O_5$ powders. As the emission of $^5D_4–^7F_5$ for Tb^{3+} (at 541 nm) was monitored, a broadband originated from the allowed f–d transition of Ce^{3+} and the weak lines associated with forbidden f–f transition of the Tb^{3+} ions were observed, which was much stronger than the excitation lines of Tb^{3+} itself (see Fig. 2(b)). This implies that efficient ET took place from Ce^{3+} to Tb^{3+} ions. According to Dexter's theory, the ET efficiency through multipolar interaction mainly depends on the overlapping extent between the emission of sensitizer and the absorption of activator. Since wide-band emission of Ce^{3+} ions and presence of many absorption lines of Tb^{3+} ions at ultraviolet region, the overlapping between Ce^{3+} emission and Tb^{3+} absorption occurs, leading to efficient ET from Ce^{3+} to Tb^{3+}. Compared with the single Tb^{3+}-doped sample (see Fig. 2(b)), the $^5D_4–^7F_5$ intensity for Tb^{3+} increases over 30 times. Because the f–f transitions for Tb^{3+} ions are electronic dipole forbidden ones, the excitation efficiency for Tb^{3+} itself is very low. However, the f–d transitions of the Ce^{3+} ions are allowed ones, the luminescence strength of Tb^{3+} in the Ce^{3+}- and Tb^{3+}-codoped $2SrO–0.25B_2O_3–0.75P_2O_5$ sample can be increased through exciting Ce^{3+}.

The dependence of the relative $^5D_4–^7F_5$ emission intensity for Tb^{3+} on the value of n in $2SrO–nB_2O_3–(1–n)P_2O_5$:1%Ce^{3+}, 2.5%Tb^{3+}powders is presented in Fig. 3. Under the excitation of 286 nm light, the intensity of Tb^{3+} varies significantly. The emission intensity of $^5D_4–^7F_5$ in the samples $n = 0.01$ and 0.90 is rather weak. As n varies from 0.10 to 0.50, the intensity becomes stronger and the intensity for the sample with $n = 0.25$ is the strongest. The emission intensity of Tb^{3+} as a function of n is deduced, respectively, to be 0.83 in the $n = 0.01$, 28.69 in the $n = 0.10$, 100 in the $n = 0.25$, 61.33 in the $n = 0.50$ and 1.22 in the

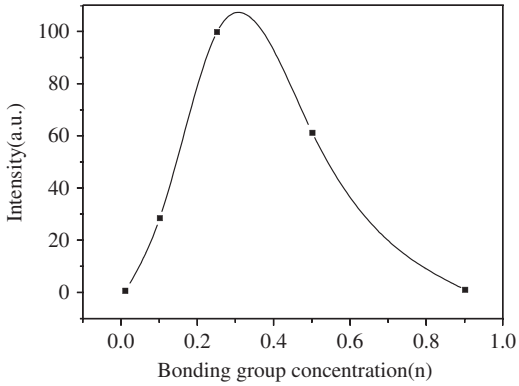

Fig. 3. The dependence of emission intensity for Tb^{3+} on the value of n in $2SrO–nB_2O_3–(1–n)\ P_2O_5$:1%$Ce^{3+}$,2.5%$Tb^{3+}$ powders ($\lambda_{em} = 541$ nm, $\lambda_{ex} = 286$ nm).

$n = 0.90$ samples. Note that in the pure Ce^{3+}-doped powders, the emission intensity of Ce^{3+} as a function of n is also determined, respectively, to be 0.85 in the $n = 0.01$, 17.23 in the $n = 0.10$, 100 in the $n = 0.25$, 74.35 in the $n = 0.50$ and 1.56 in the $n = 0.90$ samples. Similarly, the intensity in the sample with $n = 0.25$ is also the strongest. The rule of the intensity variation of Ce^{3+}on the value of n is the same as that of Tb^{3+}. The above results demonstrate that the sample with $n = 0.25$ is the optimum composition. According to the XRD patterns, the powders of $n = 0.10–0.50$ are the hexagonal space groups, while the powders of $n = 0.01$ and 0.90 are the mixed orthorhombic and monoclinic phases. Thus, we can conclude that in the hexagonal phases, the trivalent rare earths Tb^{3+} and Ce^{3+} have stronger f–d and f–f transitions and more effective ET efficiency. The ET efficiency from Ce^{3+} to Tb^{3+} should depend mainly on the excitation cross-section of Ce^{3+} (the excitation cross section is proportional to the f–d radiative transition of Ce^{3+}) and the ET rate from Ce^{3+} to Tb^{3+}, which relates to the average distance between Ce^{3+} and Tb^{3+} and the concentration of Tb^{3+}. According to the following fluorescence dynamics, the excitation cross-section of Ce^{3+} in the hexagonal phases increases relative to that in the other phases, leading to the increase of ET efficiency. The average distance between $Ce^{3+}$and Tb^{3+} might change also. The detailed reason should be discussed further.

To study the dependence of the ET efficiency between Ce^{3+} and Tb^{3+}on the value of n further, the normalized emission spectra in various $2SrO–nB_2O_3–(1–n)P_2O_5$:1%Ce^{3+},2.5%Tb^{3+} powders are shown in Fig. 4. By using the area beneath the curves, we determined the intensity ratio of Tb^{3+} to Ce^{3+} in different samples. The values of the intensity ratio of Tb^{3+} to $Ce^{3+}$are calculated, respectively, to be 0.12 in the $n = 0.01$ sample, 0.38 in the $n = 0.10$, 0.21 in the $n = 0.25$, 0.16 in the $n = 0.50$, and 0.15 in the $n = 0.90$ one. It is obvious that in the $n = 0.10$ sample, the intensity ratio of Tb^{3+} to Ce^{3+} is the largest and in the $n = 0.01$ samples the ratio is the smallest. As n varies from 0.90 to 0.10, the intensity ratio becomes larger gradually. The increased intensity ratio of Tb^{3+} to Ce^{3+} means the increased ET efficiency from Ce^{3+} to Tb^{3+}. In the $n = 0.10$ sample, the ET efficiency is the largest; and in the samples with hexagonal structure, the ET efficiency is larger than that in the other samples. The ET efficiency from Ce^{3+} to Tb^{3+} should mainly depend on the electronic transition rate of Ce^{3+} and the average distance between Ce^{3+} and Tb^{3+}. The increased electronic transition rate of Ce^{3+} should lead to the increased ET efficiency, on the contrary, the increased nonradiative electronic transition rate of Ce^{3+} should lead to the decreased ET efficiency. Compared with Fig. 3, it is interesting to observe that in the $n = 0.10$ sample, the ET efficiency is larger than that in the

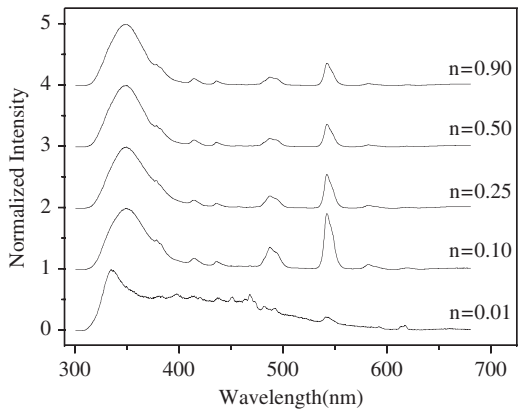

Fig. 4. The normalized emission spectra in various $2SrO–nB_2O_3–(1–n)P_2O_5$: $1\%Ce^{3+}$,$2.5\%Tb^{3+}$ powders ($\lambda_{em} = 541$ nm, $\lambda_{ex} = 286$ nm).

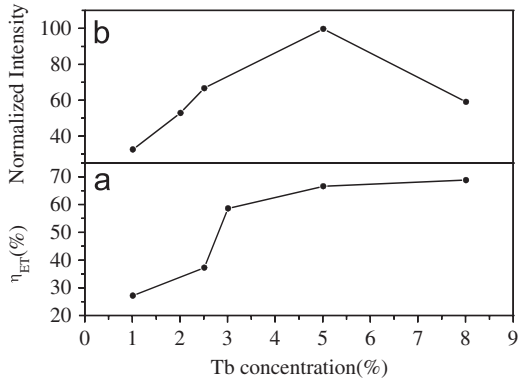

Fig. 5. (a) Dependence of ET efficiency and (b) emission intensity of Tb^{3+} on Tb^{3+} concentration (the Ce^{3+} concentration is fixed at 1%).

$n = 0.25$ sample. However, the brightness of the green emissions of $^5D_4$–$^7F_5$ was weaker than that in the $n = 0.25$ sample for the same concentrations of $Ce^{3+}$and Tb^{3+}. This could be attributed to increased nonradiative ET rate from $^5D_4$ to defect states in the $n = 0.10$ sample, which can be definitely revealed by the fluorescence dynamics of Tb^{3+}.

Fig. 5(a) and (b), respectively, show the dependence of the ET efficiency of Ce^{3+}–Tb^{3+} and the $^5D_4$–$^7F_5$ emission intensity of Tb^{3+} on the Tb^{3+} concentration in $2SrO–0.25B_2O_3–0.75P_2O_5$: Ce^{3+}/Tb^{3+}powders. The ET efficiency from a donor (Ce^{3+}) to an acceptor (Tb^{3+}) can be calculated according to the formula:

$$\eta_{ET} = 1 - \frac{I_d}{I_{d0}}, \tag{1}$$

where I_d and I_{d0} are the corresponding luminescence intensity of the donor (Ce^{3+}) in the presence and absence of the acceptor (Tb^{3+}) for the same donor (Ce^{3+}) concentration, respectively [20]. It can be seen from Fig. 5(a) that with the increase of Tb^{3+} concentration, the ET efficiency from Ce^{3+} to Tb^{3+} increases gradually. This is because the energy transfer probability from Ce^{3+} to Tb^{3+} is proportional to R^{-6} (R is the average distance between Ce^{3+} and Tb^{3+}) [21]. As the Tb^{3+} concentration increases, the average distance between Ce^{3+} and Tb^{3+} decreases. When Tb^{3+} concentration approaches to 8% in the matrix, the ET efficiency is as high as 70%. The ET between Ce^{3+} and Tb^{3+} belongs to multipolar interaction [22]. In Fig. 5(b), an intensity maximum is observed when the Tb^{3+}concentration is 5%, indicating that the quenching concentration of Tb^{3+} in $2SrO–0.25B_2O_3–0.75P_2O_5$ is around 5%. Ballman also reported that the quenching of Tb^{3+} emission occurred at the high Tb^{3+} concentration and was related to the matrix [23].

3.3. Luminescent dynamics of Ce^{3+} and Tb^3

Under the excitation of 286 nm light, the fluorescence dynamics of Ce^{3+} ions in the $2SrO–nB_2O_3–(1–n)P_2O_5$:$1\%Ce^{3+}$, $2.5\%Tb^{3+}$ samples with different n at room temperature are shown in Fig. 6. It can be seen that in the $n = 0.10$–0.50 samples, the luminescence of Ce^{3+} decays exponentially, while in the $n = 0.01$ sample, the luminescence decays bi-exponentially. And, the lifetime of Ce^{3+} becomes shorter with the decrease of n, as labeled in Fig. 6. This is attributed to the increased ET rate as well as the ET efficiency from Ce^{3+} to Tb^{3+} with the decrease of n. The bi-exponential decay curve in the $n = 0.01$ sample includes two components, a faster one and a slower one. It was well fitted by a bi-exponential function, $I = I_1 \exp(\tau_1/t_1)+I_2 \exp(\tau_2/t_2)$, with $I_1+I_2 = 1$. The fitting parameters are $I_1 = 0.28$, $\tau_1 = 1.98$ ns, $I_2 = 0.72$ and $\tau_2 = 26.44$ ns for the sample with $n = 0.01$. The average lifetime can be calculated by

$$\langle\tau\rangle = \frac{I1\tau_1^2 + I2\tau_2^2}{I1\tau_1 + I_2\tau_2}. \tag{2}$$

The average lifetime of the $n = 0.01$ sample is deduced to be 25.75 ns. The bi-exponential decay in the $n = 0.01$ sample could be attributed to two different local environments surrounding Ce^{3+} ions caused by two different phases, α-$Sr_2P_2O_7$ phase (with longer decay time constant) and $Sr_2B_2O_5$ phase (with shorter decay time constant). Note that in the sample $n = 0.90$, the luminescence dynamics of Ce^{3+} is too weak to detect. This can be attributed to largely increased nonradiative transition rate of Ce^{3+} in the monoclinic $Sr_2B_2O_5$ phase.

Fig. 7(a) shows the dependence of the exponential lifetime of the 5d–4f transitions for Ce^{3+} on the Tb^{3+}concentration in $2SrO–0.25B_2O_3–0.75P_2O_5$:$Ce^{3+}/Tb^{3+}$ powders. It is obvious that the lifetime of $^2D_{3/2}$ for Ce^{3+} ion in the samples decreases with the increasing concentration of Tb^{3+} due to the improved ET rate from Ce^{3+} to Tb^{3+}. In Ce^{3+}/Tb^{3+}co-doped samples, the reciprocal of the luminescence lifetime equals the sum of the electronic transition rate of Ce^{3+} and the ET rate of $Ce^{3+}\rightarrow Tb^{3+}$. Fig. 7(b) shows the dependence of the reciprocal of the lifetime of Ce^{3+} on Tb^{3+} concentration. It can be seen that the reverse of the lifetime of Ce^{3+} increases linearly with the increase of Tb^{3+} concentration. Therefore, the experimental points are fitted with the function:

$$\tau^{-1} \propto R_C + R_{ET}[Tb^{3+}], \tag{3}$$

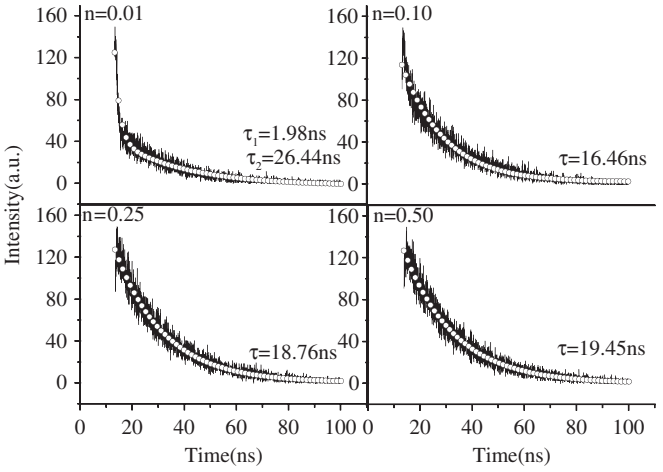

Fig. 6. The fluorescence dynamics for the $^2D_{3/2}$ of Ce^{3+} ions in the $2SrO–n$-$B_2O_3–(1–n)P_2O_5$:Ce^{3+},Tb^{3+} samples with different n at room temperature. The solid lines are the experimental data, and scattered points are the fitted curves.

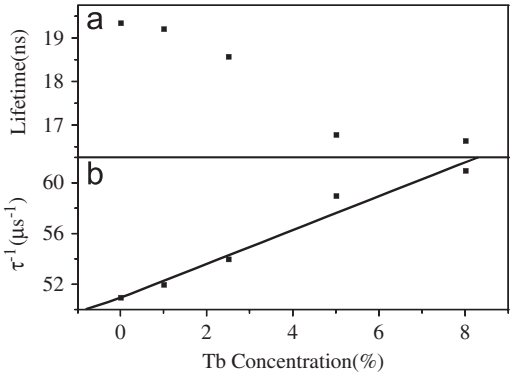

Fig. 7. (a) Dependence of Ce^{3+} lifetime and (b) the reverse of the lifetime of Ce^{3+} on Tb^{3+} concentration in $2SrO–0.25B_2O_3–0.75P_2O_5$ (the Ce^{3+} content is fixed at 1%).

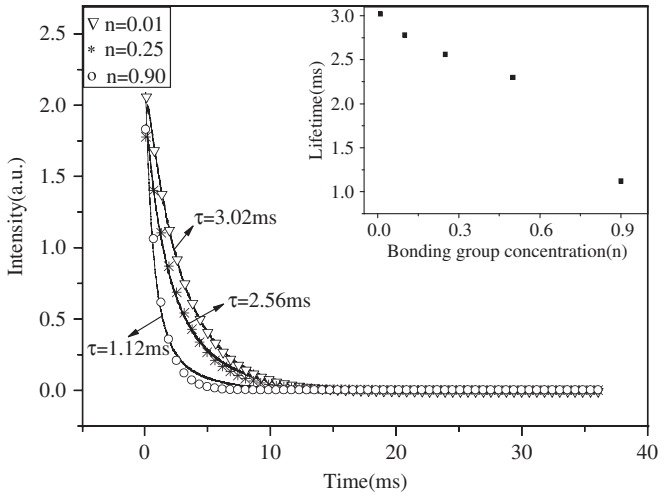

Fig. 8. Fluorescence decay curves for the $^5D_4–^7F_5$ of Tb^{3+} in different $2SrO–n-B_2O_3–(1–n)P_2O_5$:1%$Ce^{3+}$,2.5%$Tb^{3+}$ samples at 541 nm under the 355 nm excitation at room temperature ($n = 0.01$, 0.25, 0.90). The solid lines are the experimental data, and scattered points are the fitted curves. The inset shows the dependence of Tb^{3+} lifetime on different n values.

where R_C is the electronic transition of Ce^{3+}, including the radiative and nonradiative transitions, and R_{ET} is the total ET rate of $Ce^{3+} \rightarrow Tb^{3+}$, and $[Tb^{3+}]$ is the concentration of Tb^{3+}. By fitting, R_C is determined to be $5.1 \times 10^{-2}\,ns^{-1}$. R_{ET} is deduced to be $1.34\,ns^{-1}\,mol^{-1}$.

The luminescence dynamics for Tb^{3+} are also studied. Fig. 8 shows the luminescence decay curves of the $^5D_4–^7F_5$ transitions in the $n = 0.01$, 0.25 and 0.90 samples. Like the luminescence decay of Ce^{3+} in $2SrO–nB_2O_3–(1–n)\ P_2O_5$ powders, the luminescence decay of Tb^{3+} can also be fitted by the single exponential function, and the lifetime of Tb^{3+} are 3.02, 2.56 and 1.12 ms, respectively. Moreover, as shown in the inset of Fig. 8, it is obvious that the lifetime of the $^5D_4–^7F_5$ for Tb^{3+} becomes longer with the decrease of n. According to the results in Figs. 6 and 8, the luminescence lifetime of Ce^{3+} decreases with the decrease of n, while that of Tb^{3+} increases. This is attributed to the increased ET rate and more efficient ET from Ce^{3+} to Tb^{3+} with the decrease of n ($n = 0.10–0.90$).

Fig. 9 shows luminescence decay curves of the $^5D_4–^7F_5$ transitions in $2SrO–0.25B_2O_3–0.75P_2O_5$:$Ce^{3+}$/$Tb^{3+}$ powders with 0.25% and 2.5% Ce^{3+} concentrations at room temperature. The fluorescence lifetime of Tb^{3+} ($^5D_4$) is in the range of milliseconds due to the forbidden nature of the f–f transition. The $^5D_4–^7F_5$ emissions decay exponentially and the lifetimes of $^5D_4$ are

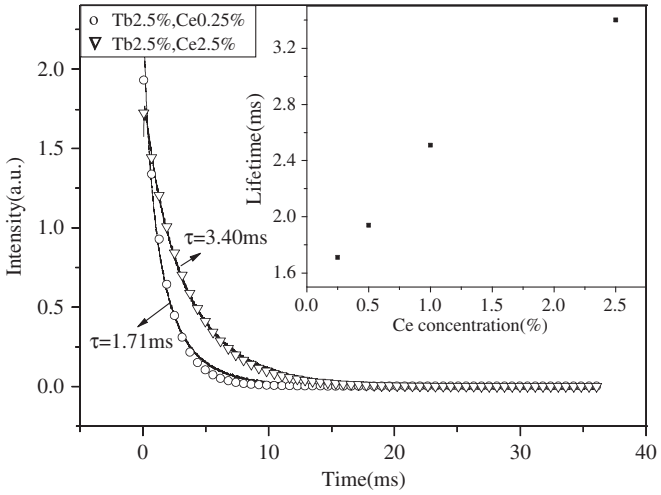

Fig. 9. Fluorescence decay curves for the $^5D_4–^7F_5$ of Tb^{3+} in the $2SrO–0.25-B_2O_3–0.75\ P_2O_5$ powders with 0.25% and 2.5% Ce^{3+} concentrations at room temperature (the Tb^{3+} content is fixed at 2.5%) ($\lambda_{em} = 541$ nm, $\lambda_{ex} = 355$ nm). The solid lines are the experimental data, and scattered points are the fitted curves. The inset shows the relation of the lifetime of Tb and different Ce concentration.

determined to be 1.71 and 3.40 ms, respectively. On the other hand, as shown in the inset of Fig. 9, it is apparent that the luminescence lifetime of Tb^{3+} increases with the increase of Ce^{3+} concentration due to the improved ET from Ce^{3+} to Tb^{3+}.

4. Conclusions

The green phosphors $2SrO–nB_2O_3–(1–n)P_2O_5$:Ce^{3+},Tb^{3+} were synthesized by the solid-state reaction. Their structural and photoluminescent properties were systematically studied. The results demonstrate that the structure of the samples with $n = 0.10–0.50$ belongs to the hexagonal phase, while the structures of the $n = 0.01$ and 0.90 samples are the mixed phases of α-$Sr_2P_2O_7$ and $Sr_2B_2O_5$. The phosphors in the hexagonal phase have much stronger brightness in contrast to the pure α-$Sr_2P_2O_7$, $Sr_2B_2O_5$ and the mixture of them. For the $2SrO–nB_2O_3–(1–n)\ P_2O_5$:$Ce^{3+}$,$Tb^{3+}$ series, the optimum composition is $2SrO–0.25-B_2O_3–0.75P_2O_5$. The efficiency of ET from $Ce^{3+}$to Tb^{3+} increases with the decrease of n and increases with the increase of Tb^{3+} concentration due to increased radiative transition rate of Ce^{3+} and decreased distance between Ce^{3+} and Tb^{3+}. The ET efficiency can reach to as high as70% in $2SrO–0.25B_2O_3–0.75P_2O_5$ and the ET rate of $Ce^{3+} \rightarrow Tb^{3+}$ is deduced to be $1.34\,ns^{-1}\,mol^{-1}$.

Acknowledgments

This work is supported by the financial supports of Nation Natural Science Foundation of China (Grant nos. 10704073, 50772042 and 10504030) and the 863 Project of China (Grant no. 2007AA032314).

References

[1] G. Blasse, B.C. Grabmaier, Lumin. Mater. 115 (1994) 140.
[2] S. Shionoya, W.M. Yen, Phosphor Handbook, vol. 391, 1999, p. 511.
[3] A.A. Vorokov, Y.A. Pyatenko, Sov. Phys. Crystallogr. 12 (1967) 214.
[4] A. Karthikeyani, R. Jagannathan, J. Lumin. 86 (2000) 79.
[5] A. Levesseur, R. Olazcuaga, M. Kbala, M. Zahir, P. Hagenmuller, M. Couzi, Solid State Ion. 9 (1981) 205.
[6] R. Kniep, H. Engelhardt, C. Hauf, Chem. Mater. 10 (1998) 2930.
[7] G. Blasse, A. Bril, J. De Vries, J. Inorg. Nucl. Chem. 31 (1969) 568.
[8] J.W.M. Verwey, G.J. Dirken, G. Blasse, J. Phys.Chem. Solids 53 (1992) 367.

[9] L.C. Nehru, K. Marimuthu, M. Jayachandran, C.H. Lu, R. Jagannathan, J. Phys. D. Appl. Phys. 34 (2001) 2599.
[10] P. Dorenbos, L. Pierron, L. Dinca, C.W.E. van Eijk, A. Kahn-Harari, B. Viana, J. Phys. Condens. Matter 15 (2003) 511.
[11] H.B. Liang, Q. Su, Y. Tao, T.D. Hu, T. Liu, S.L.E. Shulin, J. Phys. Chem. Solids. 63 (2002) 719.
[12] J. Holsa, M. Leskela, L. Niinisto, J. Solid State Chem. 37 (1981) 267.
[13] D. Jia, W. Jia, X.J. Wang, W.M. Ren, Solid State Commun. 129 (2004) 1.
[14] M. Jose, A. Lakshmanan, Opt. Mater. 24 (2004) 651.
[15] A.A. Michael, J. Electrochem. Soc. 114 (1967) 367.
[16] M. Yu, J. Lin, J. Fu, H.J. Zhang, Y.C. Han, J. Mater. Chem. 13 (2003) 1413.
[17] H.B. Liang, Q. Su, S. Lu, Y. Tao, T. Hu, T. Liu, Mater. Res. Bull. 37 (2002) 1981.
[18] Q. Zeng, N. Kilah, M. Riley, J. Lumin. 101 (2003) 167.
[19] I.V. Berezovskaya, V.P. Dotsenko, N.P. Efryushina, A.S. Voloshinovskii, C.W.E. van Eijk, P. Dorenbos, A. Sidorenko, J. Alloys Compd. 391 (2005) 170.
[20] J.C. Bourcet, F.K. Fong, J. Chem. Phys. 60 (1974) 34.
[21] K. Riwotzki, H. Meyssamy, A. Kornowski, M. Haase, J. Phys. Chem. B 104 (2000) 2824.
[22] S.J. Ding, D.W. Zhang, B.Q. Xu, J.T. Wang, J. Funct. Mater. 31 (2000) 84 (in Chinese).
[23] A.A. Ballman, Am. Mineral. 47 (1962) 1580.